




Cite this: *RSC Adv.*, 2021, **11**, 16906

# Effect of heat treatment on the microstructure and ablation performance of C/C–SiC composites containing ZrSi<sub>2</sub>–Si

Tianxing Jiang, Yi Zeng, \* Xiang Xiong, Ziming Ye, Huilin Lun, Shiyao Chen, Jinrun Hu,  Ge Yang and Sen Gao

Low-temperature reactive melt infiltration (LRMI) is advantageous for the fabrication of ceramic matrix composites (CMCs). However, residual metal in CMCs prepared by LRMI deteriorates the high-temperature properties. In this study, C/C–SiC composites containing ZrSi<sub>2</sub>–Si were prepared using LRMI at 1400 °C, and the effect of heat treatment at 1400 °C for 10, 20, or 30 h on the microstructure and ablation properties of the composites fabricated using three different ternary alloys (e.g., Zr<sub>0.047</sub>B<sub>0.0378</sub>Si<sub>0.9152</sub>, Zr<sub>0.0724</sub>B<sub>0.0366</sub>Si<sub>0.891</sub>, and Zr<sub>0.1</sub>B<sub>0.05</sub>Si<sub>0.85</sub>) was investigated. The results show that the residual Si in the composites can be decreased by volatilisation and the reaction between Si and C during heat treatment, resulting in a decrease in the density and an increase in the SiC content. The ablation rates of the composites after heat treatment for 20 h were lower than those of the samples after heat treatment for 30 and 10 h. Among the three alloys, the composites prepared using Zr<sub>0.0724</sub>B<sub>0.0366</sub>Si<sub>0.891</sub> demonstrated the best ablation performance. Their linear and mass ablation rates at 1911 °C were  $-0.11 \mu\text{m s}^{-1}$  and  $1.82 \mu\text{g s}^{-1}$ , respectively.

Received 12th March 2021

Accepted 26th April 2021

DOI: 10.1039/d1ra01971f

rsc.li/rsc-advances

## 1. Introduction

Carbon fibre-reinforced silicon carbide (C/C–SiC) is considered to be one of the most promising thermostructural materials for applications in thermal protection systems (TPSs) because of its excellent high-temperature strength, low density, good oxidation resistance, and ablation resistance.<sup>1–6</sup> NASA's X-38 aircraft uses C/C–SiC composites in the nose cone, body aileron, jaw plate, and flange. Currently, C/C–SiC composites are applied in many areas, such as rocket nozzle extension, aircraft carrier gas deflectors, thermal protection panels of near-space vehicles, space mirrors, aircraft nose cones, and engine gas rudders. Therefore, research on C/C–SiC TPSs would promote the development of aerospace applications.<sup>7–13</sup>

C/C–SiC composites can be fabricated by reactive melt infiltration (RMI),<sup>14–17</sup> which has the outstanding advantages of short preparation time, simple process, low cost, and flexibility in preparing complex parts with a dense matrix and low porosity. However, in current research,<sup>18–21</sup> the temperature of C/C–SiC composites prepared by RMI normally exceeds 1600 °C, which not only causes corrosion of the carbon fibres, thus affecting the mechanical properties of the samples, but also requires high-temperature resistant equipment.

Consequently, the low-temperature reactive melt infiltration (LRMI) process has attracted much attention because it can

reduce the preparation temperature (generally lower than 1600 °C),<sup>22–25</sup> thus removing the requirement of high-temperature resistance equipment. More importantly, it can greatly reduce the damage to carbon fibres during the preparation process, which is more conducive to industrial production. However, excessive residual metal in composites fabricated by LRMI greatly impacts the high-temperature ablation properties and high-temperature mechanical properties.<sup>16,26,27</sup> Unfortunately, few studies have focused on heat treatment to reduce residual metals and the consequent effects on the microstructure and high-temperature properties of C/C–SiC composites.

In this study, to decrease the infiltration temperature, B–Si–Zr ternary alloys with three eutectic components were chosen as the infiltration melts for LRMI. C/C–SiC composites containing ZrSi<sub>2</sub>–Si were prepared at 1400 °C by LRMI. The effects of heat treatment on the microstructure and ablation properties were investigated, and the thermal chemical ablation mechanism of the composites was examined.

## 2. Experimental procedures

### 2.1 Material preparation

A C/C preform was constructed using a needle-punched integral felt preform (the fabric structure of the preform was composed of a layer of web cloth and a layer of nonwoven cloth, and the direction of the nonwoven cloth was stacked at 0° and 90°, respectively). The C/C preform was made by using barb needles to stab the stacked carbon cloth according to a certain order,

State Key Laboratory of Powder Metallurgy, Central South University, Changsha 410083, China. E-mail: zengyi001@csu.edu.cn



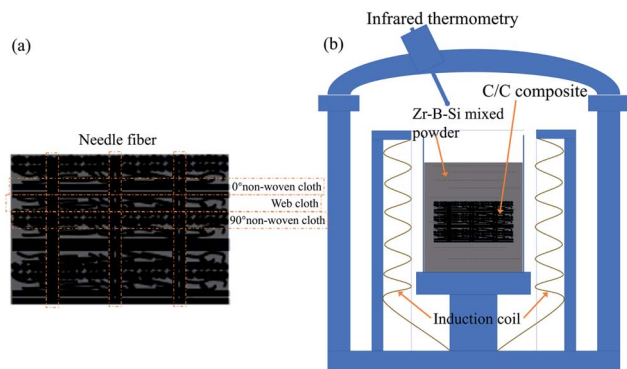


Fig. 1 Schematic of the C/C preform and LRMI process: (a) C/C preform and (b) LRMI process.

density, and penetration depth, which allowed the fibres in the mesh layer to penetrate the adjacent nonwoven cloth layers vertically, resulting in the carbon fibre preform with the density of  $0.55\text{--}0.60\text{ g cm}^{-3}$ . Pyrocarbon was then deposited by chemical vapour deposition. Finally, porous C/C composites were obtained. Then, the C/C composites were processed into  $\varnothing 29\text{ mm} \times 10\text{ mm}$  cylinders, as shown in Fig. 1(a).

According to the phase diagram of the B–Si–Zr ternary alloy, a liquid phase region appears at  $1400\text{ }^{\circ}\text{C}$  for 2–10% B, 85–92% Si, and 2–10% Zr. Three types of alloy powders were selected with increasing Zr content; they are labelled B (4.7 at% Zr, 3.78 at% B, and 91.52 at% Si), C (7.24 at% Zr, 3.66 at% B, and 89.1 at% Si), and D (10 at% Zr, 5 at% B, and 85 at% Si), respectively. All the prepared powders were milled using a zirconia ball for 24 h.

The porous C/C composites were embedded in a B–Si–Zr mixed powder and placed in a furnace. To obtain the C/C–SiC composites containing  $\text{ZrSi}_2\text{--Si}$ , the reactive infiltration temperature was raised to  $1400\text{ }^{\circ}\text{C}$  and held for 20 min. A schematic of the LRMI process is shown in Fig. 1(b). Then, the as-prepared composites were heat-treated for 0, 10, 20, and 30 h in argon atmosphere. The samples are labelled according to the alloy composition and heat-treatment time as follows: B-0 h, C-0 h, D-0 h, B-10 h, C-10 h, D-10 h, B-20 h, C-20 h, D-20 h, B-30 h, C-30 h, and D-30 h.

## 2.2 Tests and characterisation

The phase composition of the composites was investigated using a rotating-target X-ray diffraction (XRD) analyser (D/max 2550 Vb + 18 kW, Rigaku Co.) at a scanning rate of  $2^{\circ}\text{ min}^{-1}$ . The ratio of the intensities of the SiC to Si XRD peaks was calculated using software (Jade 6.0) and was used to qualitatively analyse the variation in the volume fraction of the phases. The morphology was studied using scanning electron microscopy (SEM, FEI CO., NOVA Nano230) combined with energy dispersive spectroscopy (EDS). Electron probe microanalysis (EPMA, JEOL CO, Jxa8230) was used to determine the C content and the distributions of the major elements in the carbides. The bulk density was measured using Archimedes' method. The open porosity was measured using boiling water according to ASTM Standard C20-00.

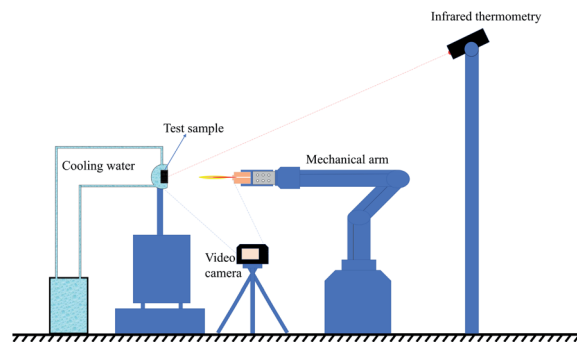


Fig. 2 Schematic of the ablation test.

The ablation resistance of the C/C–SiC composites containing  $\text{ZrSi}_2\text{--Si}$  was evaluated using air-plasma equipment<sup>28</sup> with a working current of 620 A and ablation power of 50 kW. The hydrogen flow rate was  $120\text{ L h}^{-1}$ , the argon flow rate was  $2000\text{ L h}^{-1}$ , and the inner diameter of the plasma gun tip was 4 mm. During the test, an ablation sample with a size of  $\varnothing 29\text{ mm} \times 10\text{ mm}$  was placed vertically in the flame direction in air. The distance between the gun tip and the front surface of the sample was fixed at 70 mm. Ten sample groups were tested for 200 s. The temperature of the ablated surface was monitored using an infrared thermometer, and the error was  $\pm 0.75\%$ . At the same time, the entire ablation test process was recorded using a camera (Nikon D750). A schematic of the ablation test is shown in Fig. 2. The linear ablation rate ( $R_l$ ) and mass ablation rate ( $R_m$ ) can be calculated using the following formulas:

$$R_l = \frac{d_i - d_f}{t} \quad (1)$$

$$R_m = \frac{m_i - m_f}{t} \quad (2)$$

where  $d_i$  and  $d_f$  are the initial and final thicknesses measured at the centre of the sample, respectively;  $m_i$  and  $m_f$  are the initial and final masses of the sample, respectively; and  $t$  is the test duration.

## 3. Results and discussion

### 3.1 Changes in the density and porosity of the composites before and after LRMI

Table 1 shows the bulk density and open porosity of the samples before and after LRMI at  $1400\text{ }^{\circ}\text{C}$  for 20 min. It can be seen from the table that the average initial density of the porous C/C

Table 1 Density and porosity of samples before and after LRMI for 20 min

Sample	Before LTRMI			After LTRMI		
	B	C	D	B	C	D
Density ( $\text{g cm}^{-3}$ )	1.30	1.28	1.30	2.03	2.16	2.31
Open porosity (%)	33.31	34.08	33.57	9.65	5.78	3.42



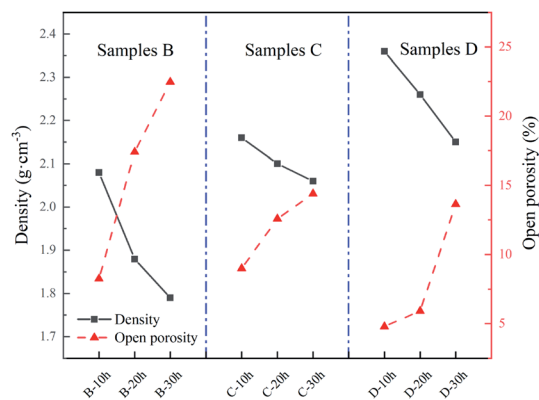


Fig. 3 Variation in the density and porosity of samples with increasing heat treatment time.

composites was  $1.29 \text{ g cm}^{-3}$ , and the porosity was above 33.00%. The average density of the composites after LRMI increased to  $2.17 \text{ g cm}^{-3}$ , and the average porosity decreased to 2.89%. Among the samples, sample D had the highest density and the lowest porosity. This is because the Zr content in the D alloy powder was the highest. Additionally, the reaction during LRMI was strongly exothermic, making it easier for the melts to infiltrate the porous C/C matrix, resulting in a highly dense sample.

As depicted in Fig. 3, the density of all the samples decreased after heat treatment, while the porosity increased with increasing heat treatment time. The density and porosity are inversely proportional. Sample D had the lowest porosity after heat treatment for 10 h. It is possible that the high Zr content in

sample D inhibited the volatilisation of Si during heat treatment. By comparison, the porosity of sample B (which had the highest Si content) had the most noticeable increase after heat treatment for 30 h owing to the highest volatilisation of Si during heat treatment.

### 3.2 Effect of heat treatment on microstructure

As shown in Fig. 4(a), the XRD patterns of the samples fabricated with three different alloys indicate that there were four main phases in the composites: C, SiC, Si, and  $\text{ZrSi}_2$ . Only small amounts of  $\text{ZrC}$  and  $\text{ZrB}_2$  were found. Clearly, most of the Zr did not convert into  $\text{ZrC}$  and  $\text{ZrB}_2$ , which have high melting temperatures ( $>3000^\circ\text{C}$ ), instead of  $\text{ZrSi}_2$ , which has a relatively low melting temperature ( $1620^\circ\text{C}$ ). The diffraction peak of the Si phase in sample B was relatively strong, while that of the  $\text{ZrSi}_2$  phase in sample D was relatively strong. The microstructures of the samples are shown in Fig. 4(b)–(d). Among the samples, the relatively high density of sample D was clearly visible in the SEM image. However, a few pores were found in samples B and C, possibly owing to the volatilisation of Si during LRMI. The content of the white phase increased in samples B, C, and D, respectively, which was mainly due to the increase in Zr content. The SEM images and XRD results clearly show that there was a large amount of residual Si in all the samples.

However, the peak intensity of SiC increased and the peak intensity of Si decreased after heat treatment, as shown in Fig. 5(a)–(c). The ratios of the peak intensities of SiC to Si are listed in Table 2. It can be concluded that the phase fraction of SiC increased with increasing heat treatment time, indicating that heat treatment is conducive to the transformation of

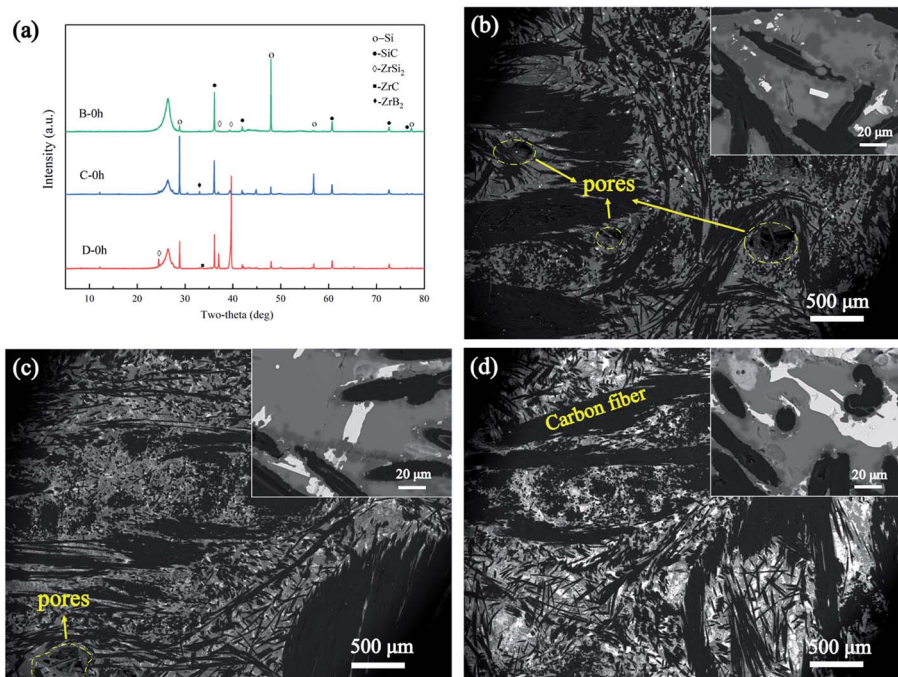


Fig. 4 Microstructure and phase analysis of samples B, C, and D prepared at  $1400^\circ\text{C}$ : (a) XRD results of samples B, C, and D, and microstructure of samples (b) B, (c) C, and (d) D.



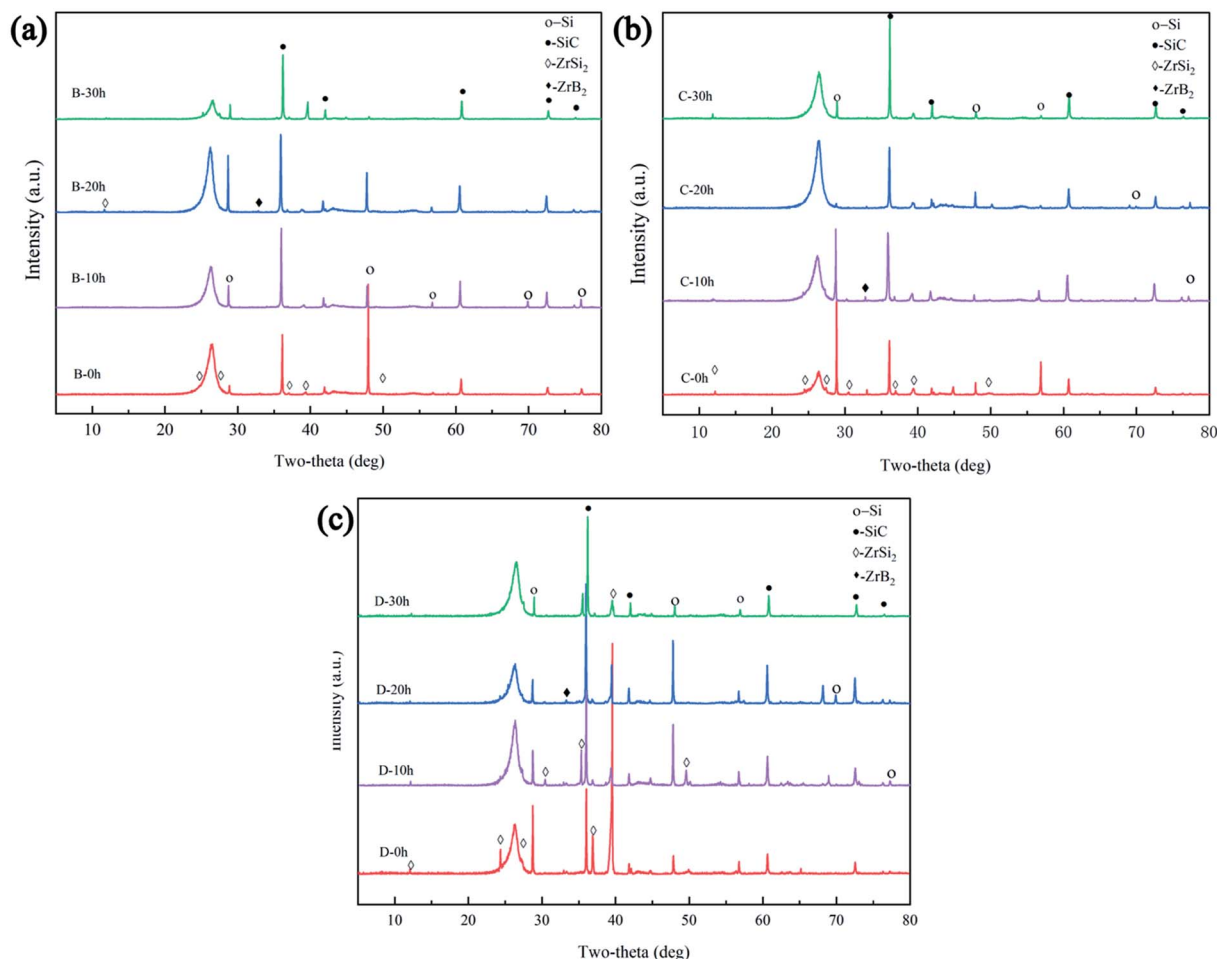


Fig. 5 XRD patterns of samples (a) B, (b) C, and (c) D after various heat treatment times.

Table 2 Ratios of SiC to Si XRD peak intensities

SiC/Si	Component B	Component C	Component D
0 h	1.02	0.81	1.43
10 h	1.51	2.96	2.78
20 h	2.05	4.48	4.04
30 h	7.19	7.74	7.46

residual Si into SiC because of the reaction between the Si and C. The peak intensity of the  $\text{ZrSi}_2$  phase in samples B, C, and D showed an increasing trend, respectively, because of the

increase in Zr content. Additionally, as shown in Fig. 6(a), Zr was mainly distributed in the white phase, C was distributed in and around the carbon fibre, and a small amount of B was distributed in the white phase, while Si is widely distributed in each phase of the composites. Elemental analysis (Table 3) in four spots verified that the dark phase is SiC, the grey phase is residual Si, and the white phase is mainly  $\text{ZrSi}_2$  with a small amount of  $\text{ZrB}_2$ .

The SEM images in Fig. 7 show the microstructural evolution of the composites, which is consistent with the XRD results. For example, when the heat treatment time of sample C increased from 0 to 30 h, the amount of SiC (shown as the dark areas in

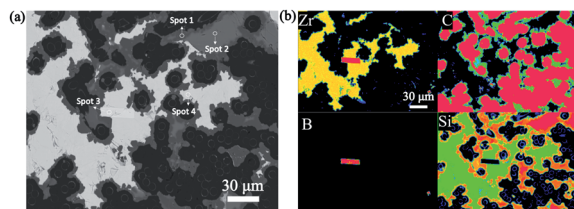


Fig. 6 EPMA of the composites after heat treatment for 20 h: (a) microstructure and (b) elemental maps.

Table 3 Composition of the ceramics in the composites after heat treatment for 20 h

	C (at%)	Si (at%)	Zr (at%)	B (at%)
Spot 1	46.6	53.37	0.03	0
Spot 2	2.65	97.31	0.04	0
Spot 3	1.63	0.14	25.26	72.97
Spot 4	3.34	64.28	32.37	0





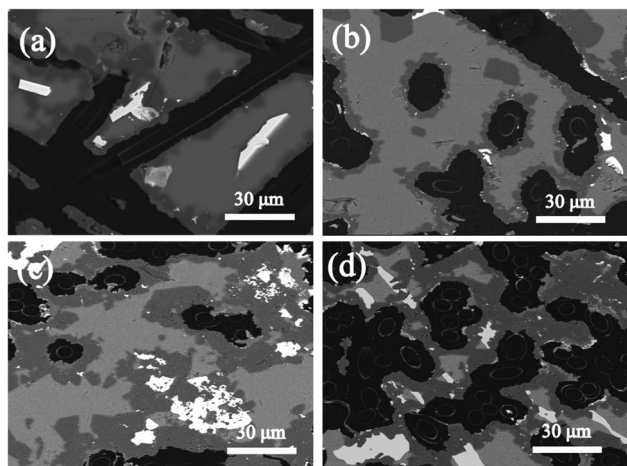


Fig. 7 SEM images of sample C: (a) C-0 h, (b) C-10 h, (c) C-20 h, and (d) C-30 h.

Fig. 7) increased; in contrast, the residual Si (shown as the grey areas in Fig. 7) decreased markedly.

### 3.3 Effect of heat treatment on ablation behaviour

Macrographs of the ablated samples are shown in Fig. 8. All ablated samples exhibit clear oxidation zones. The linear ( $R_l$ ) and mass ( $R_m$ ) ablation rates of the samples after the test are shown in Fig. 9. The ablation temperature of the samples varied because of the different emissivities of SiC, SiC, and ZrSi<sub>2</sub>. According to the comparison of the ablation properties shown in Fig. 9, the samples that were heat-treated for 20 h showed the lowest ablation rate compared with those of the other groups. In contrast, the sample heat-treated for 10 h had a higher residual Si content, which easily volatilised during the ablation process, causing more severe ablation. The sample heat-treated for 30 h had more porosity (more than 22.48%); thus, oxygen entered the substrate more easily, which eventually led to significant ablation. Furthermore, among the three samples, the ablation rate of sample C was lower than those of samples B and D. This

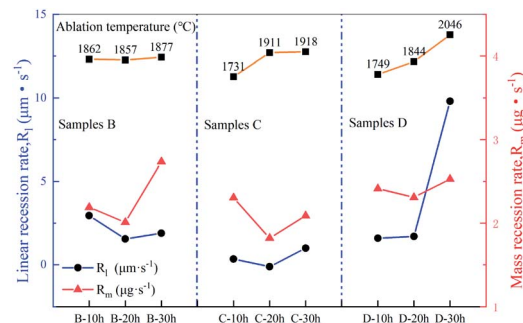


Fig. 9 Variation in linear and mass recession rates of samples B, C and D with heat treatment time.

is because the relative content of SiC was the highest in sample C. As for sample D, the ablation rate was slightly higher than that of sample C because of the relatively higher content of ZrSi<sub>2</sub> in sample D. This was possibly due to the relatively low melting temperature of the ZrSi<sub>2</sub> phase, which was insufficient to withstand the high flux plasma scouring and oxidation during the ablation process, thus resulting in damage to the matrix structure.

XRD phase analysis was performed on the ablated sample surface, as shown in Fig. 10. The surface of the ablated sample was mainly composed of ZrO<sub>2</sub>, SiO<sub>2</sub>, and SiC. As shown in Fig. 11(a)–(c), there are three main phases on the surface of the ablated samples: dark grey, light grey, and tortoise shell white phases. According to the EDS analysis, the dark grey phase (spot 1) is SiO<sub>2</sub>, the light grey phase (spot 2) is the solid solution phase of ZrO<sub>2</sub>–SiO<sub>2</sub>, and the turtle shell white phase (spot 3) is ZrO<sub>2</sub> which comes from the oxidation products of ZrSi<sub>2</sub> and ZrB<sub>2</sub>. The ZrB<sub>2</sub> can provide good ablation resistance. During the ablation process, the ZrB<sub>2</sub> reacts with oxygen to form ZrO<sub>2</sub>. The ZrO<sub>2</sub> has high viscosity at high temperature (about 2000 °C) and leaves on the surface of composite, which can act as an effective barrier against the inward diffusion of oxygen. According to the XRD and EDS results, the main thermal chemical reactions involved in the ablation process can be summarised as follows:

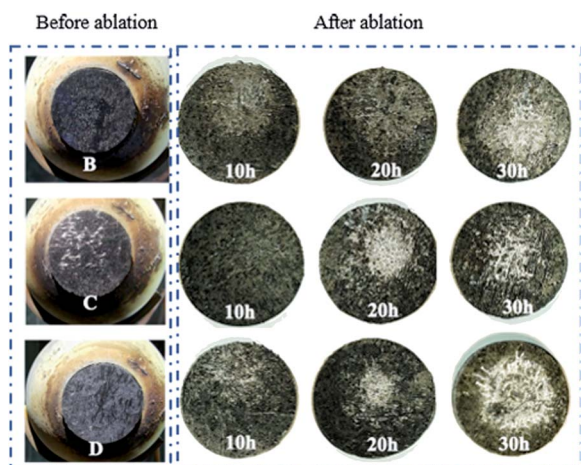


Fig. 8 Macrographs of samples before and after ablation.

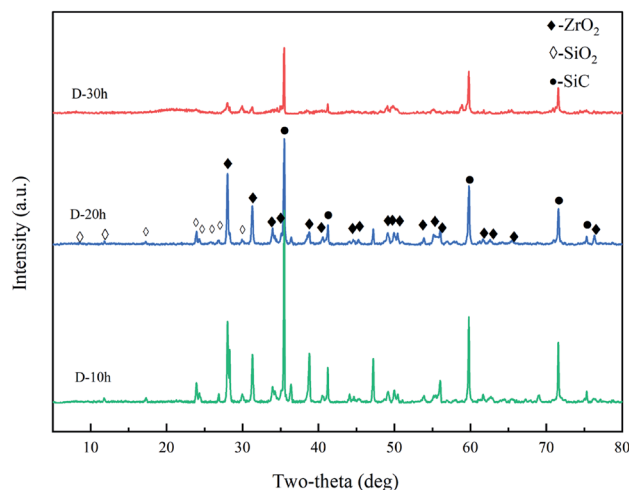


Fig. 10 XRD diffraction patterns.



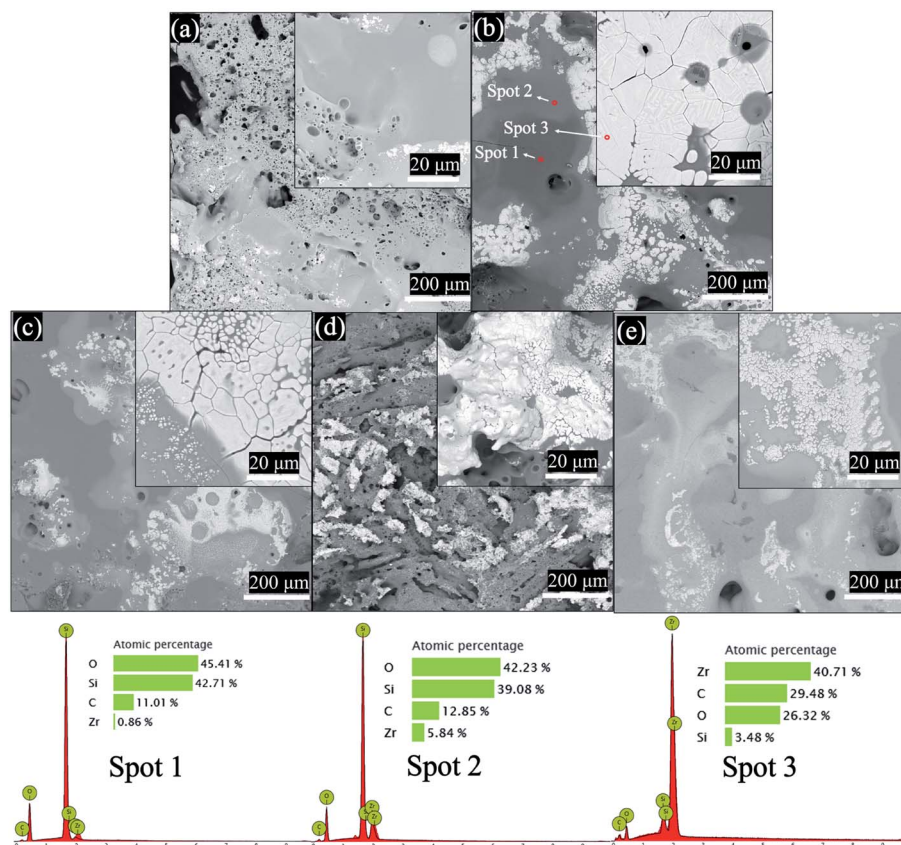
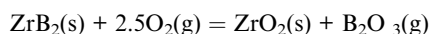
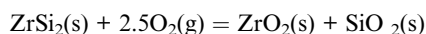
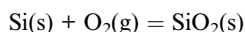
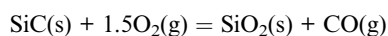
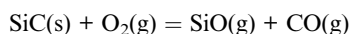
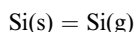
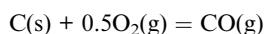


Fig. 11 Surface morphology of the ablated samples: (a) B-20 h, (b) D-20 h, (c) C-20 h, (d) C-10 h, and (e) C-30 h.



- (3) treatment with higher residual Si will have higher ablation rate.
- (4) Therefore, the samples without heat treatment have not been tested for ablation performance.
- (5) Sample C-30 h, with a porosity of nearly 15%, had many pores. Thus, the oxide layer formed during the ablation process was easily destroyed, and the pores expanded as the ablation process progressed, resulting in deep oxidation of the sample.
- (6) Similarly, compared to sample C, samples B and D had more residual Si and  $\text{ZrSi}_2$ , respectively.
- (7) During the ablation process, the non-volatile residual Si and  $\text{ZrSi}_2$  will react with  $\text{O}_2$  to form  $\text{SiO}_2$  and  $\text{ZrO}_2$ . The dense  $\text{SiO}_2$  and  $\text{ZrO}_2$  covering in surface of samples resulted in a strong oxygen resistance.
- (8) However, for B and D samples, the oxide protective layer was destroyed by excessive volatilization of residual Si and  $\text{ZrSi}_2$ , which led to poor ablation resistance of B and D samples.
- (9) Therefore, sample C-20 h exhibited the best ablation resistance. The linear and mass ablation rates at  $1911^\circ\text{C}$  were  $-0.11\ \mu\text{m s}^{-1}$  and  $1.82\ \mu\text{g s}^{-1}$ , respectively.

Comparing Fig. 11(c)–(e), there is a smooth oxide layer ( $\text{ZrO}_2\text{--SiO}_2$ ) with a small number of pores on the surface of sample C-20 h. This type of ablation morphology is mainly caused by thermal chemical ablation of high-flux heat. During the initial stage of ablation, the surface of the sample was oxidised at high temperatures, and a dense oxide layer ( $\text{ZrO}_2\text{--SiO}_2$ ) with good protection was rapidly formed on the sample.<sup>28–30</sup> As ablation progressed, some residual Si was exposed to the high-flux heat, which caused considerable volatilisation and oxidation. Therefore, large holes appeared on the surface of sample C-10 h, which had a higher content of residual Si, compared to that of sample C-20 h. Similarly, the samples without heat

## 4. Conclusions

Three B–Si–Zr alloys (which have three eutectic components) were used to prepare C/C–SiC composites containing  $\text{ZrSi}_2$ –Si using LRMI at  $1400^\circ\text{C}$ . The phases mainly comprised C, SiC, Si, and  $\text{ZrSi}_2$ . After heat treatment, the density decreased, while the porosity increased with increasing heat treatment time. Among the three alloys, a higher Zr content resulted in a higher density



of the composite. With increasing heat treatment time, the fraction of the ceramic phase (*i.e.*, SiC) increased, and that of the metal phase (*i.e.*, Si) decreased. In addition, the volatilisation of the metal phase during heat treatment caused a large number of pores to appear in the matrix. The ablation performance of the sample subjected to heat treatment for 20 h was better than those of the samples subjected to heat treatment for 10 and 30 h. The composite labelled sample C was prepared using the alloy  $\text{Zr}_{0.0724}\text{B}_{0.0366}\text{Si}_{0.891}$  and showed the lowest ablation rates. Its linear and mass ablation rates at 1911 °C were  $-0.11 \mu\text{m s}^{-1}$  and  $1.82 \mu\text{g s}^{-1}$ , respectively.

## Conflicts of interest

The authors declare that they have no known competing financial interests or personal relationships that could have appeared to influence the work reported in this paper.

## Acknowledgements

This work was supported by the National Natural Science Foundation of China [grant numbers 51602349], Innovation-Drive Project of Central South University.

## References

- 1 R. Naslain, A. Guette, F. Rebillat, L. Pailler and X. Bourrat and, *Opt. Commun.*, 2004, **449**–456.
- 2 M. T. Besmann and W. B. Sheldon and, *Science*, 1991, **1104**–1109.
- 3 S. Schmidt, S. Beyer, H. Knabe, H. Immich, R. Meistring and A. Gessler, *Acta Astronaut.*, 2004, **55**, 409–420.
- 4 T. Ishikawa, S. Kajii, K. Matsunaga, T. Hogami and Y. Kohtoku, *Science*, 1998, **282**, 1295.
- 5 W. Krenkel and F. Berndt, *Mater. Sci. Eng., A*, 2005, **412**, 177–181.
- 6 M. C. Halbig, J. D. McGuffin-Cawley, A. J. Eckel and D. N. Brewer, *J. Am. Ceram. Soc.*, 2010, **91**, 519–526.
- 7 J. E. Sheehan, K. W. Buesking and B. J. Sullivan, *Annu. Rev. Mater. Res.*, 1994, **24**, 19–44.
- 8 E. Fitzer, *Carbon*, 1987, **25**, 163–190.
- 9 S. R. Dhakate, T. Aoki and T. Ogasawara, *Adv. Mater. Lett.*, 2011, **47**, 236.
- 10 E. L. Corral and R. E. Loehman, *J. Am. Ceram. Soc.*, 2010, **91**, 1495–1502.
- 11 D. D. Jayaseelan, R. G. d. Sá, P. Brown and W. E. Lee, *J. Eur. Ceram. Soc.*, 2011, **361**–368.
- 12 Q. Fu, L. Zhuang, Q. Ren, L. Feng, H. Li and Y. Guo, *J. Materiomics*, 2015, **1**, 245–252.
- 13 Y. C. Zhu, S. Ohtani, Y. Sato and N. Iwamoto, *Carbon*, 2000, **38**, 501–507.
- 14 W. Guo, Y. Ye, S. Bai, L. Zhu, X. An and S. Li, *Ceram. Int.*, 2020, **46**, 5586–5593.
- 15 Y. Tong, S. Bai, Q. H. Qin, H. Zhang and Y. Ye, *Ceram. Int.*, 2015, **41**, 4014–4020.
- 16 J. P. Wang, M. Lin, Y. H. Zhang, Z. Xu and Z. H. Jin, *Mater. Sci. Forum*, 2008, **620–622**, 371–374.
- 17 Y. Tong, S. Bai, X. Liang, Q. H. Qin and J. Zhai, *Ceram. Int.*, 2016, **17174**–17178.
- 18 S. Hanzawa, *J. Mater. Sci.*, 2012, **47**, 833–844.
- 19 W. Guo, S. Bai and Y. Ye, *J. Eur. Ceram. Soc.*, 2020, **2347**–2355.
- 20 J. Si-Zhou, X. Xiang, C. Zhao-Ke, X. Peng and H. Bai-Yun, *Mater. Des.*, 2009, **30**, 3738–3742.
- 21 W. Guo, S. Bai, Y. Ye, L. Zhu and S. Li, *Int. J. Appl. Ceram. Technol.*, 2019, **16**, 88–96.
- 22 L. Liu, L. Zhang, W. Feng, J. Li, Y. Bai, D. Tao, X. Su, Y. Cao, T. Bao and J. Zheng, *Ceram. Int.*, 2020, **46**, 8469–8472.
- 23 Y. Zhu, S. Wang, H. Chen, W. Li, J. Jiang and Z. Chen, *Ceram. Int.*, 2013, **59**, 9085–9089.
- 24 S. Zhang, S. Wang, W. Li, Y. Zhu and Z. Chen, *Mater. Lett.*, 2012, **78**, 81–84.
- 25 C. Xiong, T. Li, T. Zhao, M. Khan, J. Wang, X. Ji, H. Li, W. Liu and Y. Shang, *Ceram. Int.*, 2015, **1057**–1062.
- 26 C. Yan, R. Liu, Y. Cao, C. Zhang and D. Zhang, *Corros. Sci.*, 2014, **86**, 131–141.
- 27 P. G. Karandikar, J. R. Singh and C. A. Andersson, *Low CTE metal-ceramic composite articles, and methods for making same*, 2007.
- 28 C. Si'an, Z. Changrui, Z. Yudi, Z. Dan and H. Haifeng, *Corros. Sci.*, 2013, **168**–175.
- 29 Z. Li, H. Li, S. Zhang and K. Li, *Ceram. Int.*, 2012, **38**, 3419–3425.
- 30 X. Chen, Q. Feng, H. Zhou, S. Dong, J. Wang, Y. Cao, Y. Kan and D. Ni, *Corros. Sci.*, 2018, **134**.

